Title
Investigation of Airfoil Parameterizations and Optimization for Rotor Broadband Noise Reduction

Journal
Vertical Flight Society 80th Annual Forum and Technology Display

Authors
Won, J
Lee, S

Publication Date
2024

Investigation of Airfoil Parameterizations and Optimization for Rotor Broadband Noise Reduction

Jordon Won
PhD Student

Seongkyu Lee
Professor

University of California, Davis
Davis, California, USA

ABSTRACT

Airfoil optimization for rotor blades is a critical endeavor aimed at enhancing aerodynamic performance and reducing noise. This paper employs a Kriging surrogate model combined with a multi-objective genetic algorithm to optimize thrust, power, and broadband noise. Three airfoil parameterization methods including ParFoil, PARSEC, and CST are compared when used to generate various airfoil shapes for the surrogate model and optimization process. We utilize low-fidelity aerodynamic tools such as XFOIL and blade element momentum theory for aerodynamics. In addition, acoustic modeling is conducted using Lee's wall pressure spectrum model alongside Amiet's trailing-edge noise model. The paper focuses on small-scale rotor configurations, specifically an ideally twisted rotor using the NACA 0012 airfoil and a modified XV-15 blade. Both blades are used as baseline models for hover optimization. The optimization of the ideally twisted rotor across various parameterization methods demonstrates a significant reduction in A-weighted overall sound pressure level by approximately 4.0 dBA. The primary contributors to this noise reduction are identified as a decrease in the chordwise pressure gradient and wall shear stress, which are key factors that contribute to the wall pressure spectrum and resulting trailing-edge noise. Similarly, the optimization of the modified XV-15 blade using the ParFoil method achieves a notable decrease in noise of 3.5 dBA. Further analysis is extended to axial flight conditions, with axial velocities of 5.0, 10.0, and 20.0 m/s, to simulate vertical climb. The results show that these hover-optimized blades are capable of sustaining noise decreases of 3.0-4.0 dBA compared to the baseline, provided that the thrust coefficient is maintained through adjustments in collective pitch.

INTRODUCTION

Optimization of rotorcraft blades is pivotal to enhance performance and manage trade-offs among several important metrics (Refs. 1, 2). For example, thrust, power, and noise play crucial roles in rotorcraft design. Typically, maximizing the rotor thrust or minimizing the power are primary concerns. Additionally, for urban air mobility vehicles (UAM), addressing rotor noise is crucial to gaining acceptance in urban communities. Considering the dimension and operation of UAM vehicles, there is a pronounced emphasis on mitigating mid to high-frequency broadband noise since such noise is especially annoying to humans.

Rotor broadband noise prediction is a burgeoning research area. Lee et al. (Ref. 3) provided an exhaustive review of airfoil trailing-edge noise, which is a prominent contributor to rotor broadband noise. The Amiet trailing-edge noise theory, which is rooted in Curle's acoustic analogy, has been used to make precise predictions of rotor trailing-edge noise (Ref. 4). Notably, Li and Lee (Refs. 5, 6) have employed low-fidelity aerodynamic methods in conjunction with the Amiet and a recently developed semi-empirical wall pressure spectrum model (Ref. 7) to successfully predict broadband noise spanning from small-scale to UAM-sized rotors. However, these studies primarily centered around noise predictions for pre-existing rotor blades without considering the aspect of design. Given this context, harnessing these validated prediction approaches for rotor blade design and optimization emerges as a pertinent course of action.

Researchers conducted studies on the optimization of helicopter blades, focusing on enhancing rotor thrust and reducing power requirements (Refs. 8, 9). These investigations employed ParFoil, which is an airfoil parameterization technique using a reference or baseline airfoil (Ref. 8). The parameters adopted airfoil attributes such as camber, camber crest position, thickness, thickness crest position, leading-edge radius, trailing-edge camber, trailing-edge camber crest position, and boat-tail angle. Given a baseline airfoil geometry, these parameters can be adjusted to yield modified airfoil designs. In these studies, ParFoil demonstrated its capability to generate airfoils, which significantly reduce power requirements when operating in either hover or forward flight conditions when used in an optimization workflow. In addition, ParFoil has been utilized for noise reduction purposes. A study by Liu and Lee (Ref. 10) employed ParFoil to assess the influence of parameter scaling on the turbulent boundary layer, subsequently impacting the trailing-edge noise level. The findings indicated that factors such as thickness, trailing-edge camber, and boat-tail angle play pivotal roles in sound pressure level (SPL) al-

Presented at the Vertical Flight Society 80th Annual Forum & Technology Display, Montréal, Canada, May 7–9, 2024.

terations. The importance of airfoil shape for trailing-edge noise was also addressed in reference (Ref. 11). In addition, Liu and Lee (Ref. 12) combined ParFoil, Kriging surrograte model, and Genetic Algorithm (GA) optimization in conjunction with Howe's trailing-edge model (Ref. 13) to determine optimized low-noise 2-D airfoils. However, this investigation focused on 2D airfoils rather than complete rotor blades.

In a recent study by Karimian et al. (Ref. 14), the PARSEC parameterization method was adopted (Ref. 15) for airfoil shape optimization to minimize propeller noise. PARSEC employs polynomial functions to delineate the upper and lower surfaces of an airfoil, constraining them using intuitive parameters like curvature, thickness, and crest position. In their study, Amiet's trailing edge noise model was used to predict broadband noise, where they found a trailing-edge noise reduction of approximately 2.7 dB while maintaining similar aerodynamic performance.

Beyond the previously mentioned ParFoil and PARSEC methods, the Class/Shape Function Transformation (CST) method has also gained traction in airfoil optimizations mainly for aerodynamics. The CST methodology offers robust airfoil parameterization, employing a class function to classify the airfoil type and a shape function to define the airfoil surface using Bernstein polynomials (Ref. 16). The CST's flexibility arises from the degree of Bernstein polynomial adopted; higher-degree polynomials can craft more intricate shapes. Kou et al. (Ref. 17) used the CST method along with Amiet's theory to optimize airfoils for wind turbine noise. They found that airfoils that are thinner near the leading edge and thicker near the trailing edge reduced the A-weighted overall sound pressure level (OASPL(A)). Using 2D analysis, they achieved a noise reduction of approximately 1.75 dBA, when compared to the baseline NACA 0012 airfoil at angles of attack from 0° to 4°.

As the development of UAM vehicles intensifies, so too does the interest in rotor blade design for minimizing broadband noise. Thuman et al. (Ref. 18) used artificial neural networks and low-fidelity models to predict and understand which design parameters affect tonal and broadband noise. Broadband OASPL was predicted using the Brooks, Pope, and Marcolini (BPM) model (Ref. 19) and was found to be most sensitive to rotation rate and rotor radius due to its effects on the tip Mach number and Reynolds number. In addition, Ingraham et al. (Ref. 20) conducted an optimization on the X-57 Maxwell propeller subject to a fixed thrust value and revealed similar trends. While this study focused on tonal noise, it was found that when propeller rotation rate and diameter are considered in addition to chord and twist distributions, the rotation rate and diameter become the dominant features to reduce noise. In addition, to maintain the thrust with a reduced rotation rate, it was found that increasing chord length and twist were necessary. Specifically, the inboard chord length was significantly increased, resulting in a modification of the radial thrust distribution with more thrust inboard and less outboard.

The focus of this paper is broadband noise reduction through optimization of airfoil shapes. As mentioned previously, there are multiple airfoil parameterization methods where each presents unique strengths and drawbacks due to their intrinsic functionalities. Therefore, we aim to evaluate the efficacy of each airfoil parameterization within a low-fidelity multi-objective optimization framework that is developed in this study, accounting for thrust, power, and noise. In addition, the resulting optimized airfoils from each method are compared to understand what geometric and boundary layer features drive the greatest noise reduction.

METHODS

Aerodynamic and Aeroacoustic Predictions

This paper uses Blade Element Momentum Theory (BEMT) and XFOIL (Ref. 21) for aerodynamic analysis. Each blade is segmented into 100 uniformly spaced sections, wherein angle of attack and velocity are determined. Airfoil polars, acquired from XFOIL, inform the computation of thrust and power within BEMT. The primary aeroacoustic tool is UCD-QuietFly, which was previously demonstrated to effectively predict broadband noise for various rotors (Refs. 5, 6, 22). For such analyses, the rotor is partitioned into 21 uniformly spaced sections, facilitating the extraction of trailing edge boundary layer properties. The boundary layer properties are the inputs for Lee's semi-empirical wall pressure spectrum model (Ref. 7). This model was shown to accurately predict the wall pressure spectrum for both zero, adverse, and favorable pressure gradient flows for cases without flow separation. Using the angle of attack and velocity distributions determined from BEMT, the boundary layer properties such as displacement thickness and momentum thickness are calculated by XFOIL and extracted from the 99% chord location. In turn, the wall pressure spectrum is used in Amiet's trailing-edge model.

Microphone Locations Two rotors are selected for the blade optimization study: the ideally twisted rotor and the XV-15 tilt rotor. Pettingill et al. (Ref. 23) performed experiments on the ideally twisted rotor, which features a constant chord NACA 0012 airfoil with various pitch angles and RPM values. The radial angle distribution of the blade is illustrated in Fig. 1(a), while the microphone locations employed for broadband noise measurement are depicted in Fig. 1(b). Within this study, results from microphone location 5 serve as the benchmark against which optimized outcomes are compared. The optimization for the ideally twisted rotor only involves the airfoil shape at radial locations $r/R = 0.7 - 1.0$ because the higher velocity tip sections are the main contributor to trailing-edge noise. The original NACA 0012 is kept for the radial locations $r/R = 0.0 - 0.7$. The Reynolds and Mach numbers for this tip section are approximately 200,000 and 0.27 respectively.

The original XV-15 blade spans approximately 3.81 meters and rotates at 582 RPM, leading to a tip Mach number of 0.69 and a Reynolds number of approximately 5.0×10^6. Since

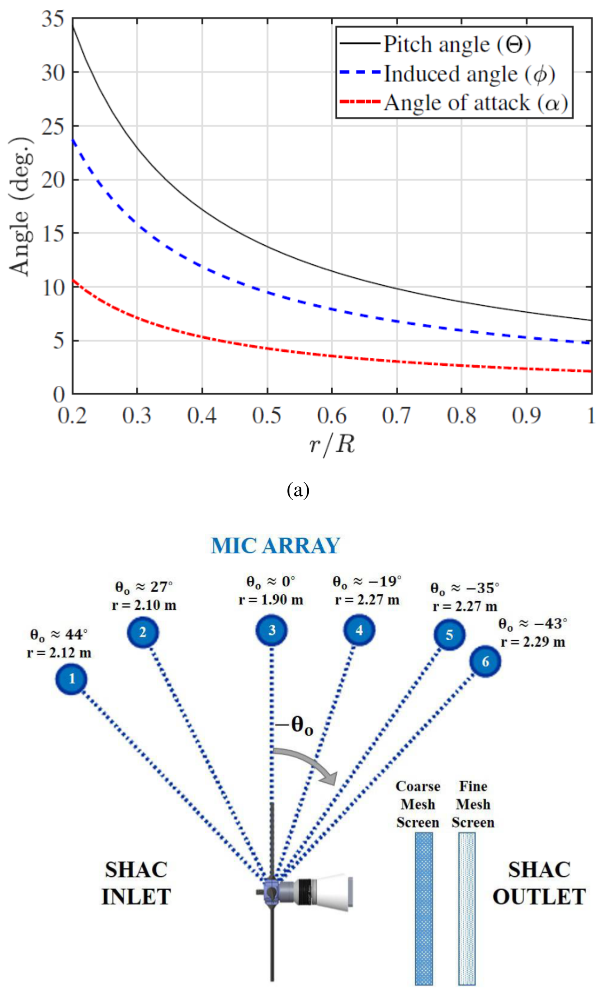

Figure 1: Ideally twisted rotor setup (Ref. 23): (a) spanwise angle distributions and (b) microphone locations.

this tip Mach number is much higher than for typical UAM rotors, this study's optimized XV-15 blade has been resized to a radius of 1.9 meters with a Mach and Reynolds number of approximately 0.34 and 1.3×10^6. This shortened blade still retains its original solidity and linear twist of -40.25 degrees. The blade is modeled with the chord and airfoil distribution shown in table 1, where the first 25% of the blade tapers linearly and the remaining 75% has a constant chord length. The real XV-15 rotor uses a thicker airfoil than the NACA 64-118 for the inboard sections. However, XFOIL is found to have convergence issues with thicker airfoils. Since the inboard sections do not significantly affect the aerodynamics and acoustics, the inboard sections are modeled with the NACA 64-118. No airfoil interpolation is used at the transition regions.

The chosen microphone location for optimization is positioned 270 degrees relative to the rotor plane and set at a distance equivalent to 40 rotor radii. Given the critical importance of the blade's outboard sections for both aerodynamic efficiency and acoustic characteristics, the study's optimization focuses on the sections where $r/R = 0.7 - 1.0$. A dual-

Table 1: Modeled XV-15 chord and airfoil distribution

r/R	**Chord (m)**	**Airfoil**
0.00-0.25	$0.5021 - 0.5859 \times r/R$	NACA 64-118
0.25-0.70	0.3556	NACA 64-118
0.70-0.90	0.3556	NACA 64-(1.5)12
0.90-1.00	0.3556	NACA 64-208

airfoil optimization strategy is adopted: Airfoil 1 covers the range $r/R = 0.7 - 0.9$, and Airfoil 2 spans $r/R = 0.7 - 0.9$.

Airfoil Parameterization Methods

The ideally twisted rotor in hover serves as a platform to investigate the differences and similarities among ParFoil, PARSEC, and CST airfoil parameterization methods. For the optimization of the XV-15, only the ParFoil method is employed.

ParFoil ParFoil, as detailed in (Refs. 8,9,24), is a morphing-based airfoil parameterization method where the coordinates of a baseline airfoil are adjusted to scale specific features. The parameters utilized by ParFoil are depicted in Fig. 2. In this method, users can independently modify the leading and trailing-edge sections of the airfoil, designated as y_R, and can define a location, y_B, to measure the boat-tail angle. For the purposes of our study, these parameters are fixed at $x/c = 0.6$ and $x/c = 0.8$, respectively. Initially, the baseline airfoil parameters, such as the leading-edge radius (k), camber (m), location of the leading-edge camber crest (x_0), thickness (t), location of the thickness crest (p_0), trailing-edge camber (n), location of the trailing-edge camber crest (q), and the boat-tail angle (b), are computed. These values are then modified according to user inputs, either scaled or shifted. If the airfoil is symmetric, a minor camber line is incorporated, which can also be adjusted according to user specifications.

In the optimization of the ideally twisted rotor using ParFoil, only seven parameters are selected for adjustment: leading-edge radius scaling factor (k), camber scaling factor (m), leading-edge camber crest position (x_0), thickness scaling factor (t), trailing-edge camber (n), trailing-edge camber crest position (q), and boat-tail angle factor (b). Notably, the leading-edge camber crest location (x_0) is assumed to coincide with the thickness crest location (p_0), simplifying the parameterization process. Figure 3 illustrates the upper and lower bounds of these parameters, providing a visual comparison against the baseline NACA 0012 airfoil.

PARSEC PARSEC is a popular airfoil parameterization method that uses three control points to create a curve for each surface (Refs. 15, 25, 26). Figure 4 shows the 11 parameters for PARSEC.

The user can alter the leading-edge radius (r_{le}), thickness crest position (x_s), thickness (z_s), curvature (z_{xxs}), and trailing-edge

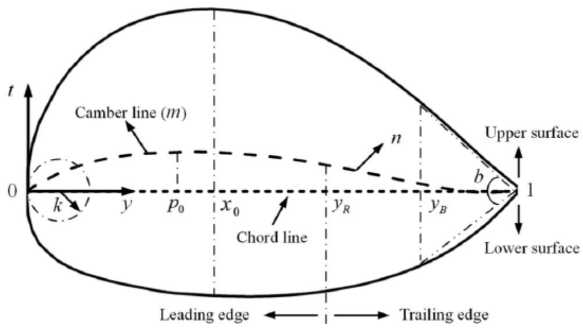

Figure 2: Diagram of ParFoil parameters (Ref. 10).

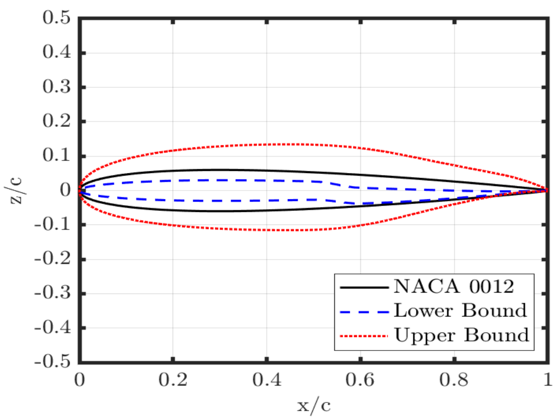

Figure 3: ParFoil upper and lower bound of airfoil design space.

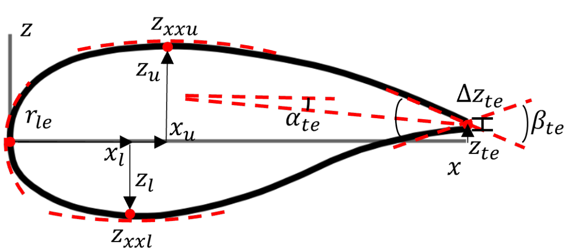

Figure 4: Diagram of PARSEC parameters.

location (z_{te}), thickness (Δz_{te}), direction (α_{te}), and wedge angle (β_{te}). Here, the subscript s represents either the upper or lower surface. The equation used to create each surface is

$$z_s = \sum_{i=1}^{n=6} a_s \cdot x^{\frac{i-1}{2}}. \tag{1}$$

The coefficients a_s are found by solving the $C_s a_s = b_s$, where C_s is equal to

$$\begin{bmatrix} 1 & 1 & 1 & 1 & 1 & 1 \\ x_s^{1/2} & x_s^{3/2} & x_s^{5/2} & x_s^{7/2} & x_s^{9/2} & x_s^{11/2} \\ 1/2 & 3/2 & 5/2 & 7/2 & 9/2 & 11/2 \\ \frac{1}{2}x_s^{-1/2} & \frac{3}{2}x_s^{1/2} & \frac{5}{2}x_s^{3/2} & \frac{7}{2}x_s^{5/2} & \frac{9}{2}x_s^{7/2} & \frac{11}{2}x_s^{9/2} \\ -\frac{1}{4}x_s^{-3/2} & \frac{3}{4}x_s^{-1/2} & \frac{15}{4}x_s^{1/2} & \frac{35}{4}x_s^{3/2} & \frac{63}{4}x_s^{5/2} & \frac{99}{4}x_s^{7/2} \\ 1 & 0 & 0 & 0 & 0 & 0 \end{bmatrix}, \tag{2}$$

and

$$b_{upper} = \begin{bmatrix} z_{te} + \frac{1}{2}\Delta z_{te} \\ z_{up} \\ \tan(\frac{2\alpha_{te} - \beta_{te}}{2}) \\ 0 \\ Z_{xxup} \\ \sqrt{r_{le}} \end{bmatrix}, b_{lower} = \begin{bmatrix} z_{te} - \frac{1}{2}\Delta z_{te} \\ z_{lo} \\ \tan(\frac{2\alpha_{te} + \beta_{te}}{2}) \\ 0 \\ Z_{xxlo} \\ \sqrt{r_{le}} \end{bmatrix}. \tag{3}$$

Equation 1 is simply a polynomial that is formulated to go through three points: the leading edge, trailing edge, and thickness crest location.

For this study, all parameters from the PARSEC model are utilized except for the trailing-edge coordinate and thickness (9 parameters in total). These parameters are fixed at $z_{te} = 0.0$ and $\Delta z_{te} = 0.00252$, respectively, aligning with the values used for the NACA 0012 airfoil. Unlike ParFoil, which requires baseline airfoil coordinates for morphing, PARSEC can generate airfoils solely based on its parametric values. This capability allows for the creation of diverse airfoil shapes directly from the specified parameters without the need for an initial geometric template. However, to ensure that the optimization results from PARSEC are comparable to those from ParFoil, the parameter bounds used in the optimization process are centered around the PARSEC alues that yield an airfoil closely resembling the NACA 0012. The specific values for these parameters are determined using least-squared fitting and are shown in Eq. (4). Figure 5 contrasts the baseline NACA 0012 to airfoils that are generated using the upper and lower bound values selected.

$$\begin{bmatrix} r \\ x_u \\ z_u \\ z_{xx_u} \\ x_l \\ z_l \\ z_{xx_l} \\ \beta \\ \Delta z_{te} \\ \alpha \\ z_{te} \end{bmatrix} = \begin{bmatrix} 0.0146 \\ 0.3009 \\ 0.0600 \\ -0.4404 \\ 0.3009 \\ -0.0600 \\ 0.4404 \\ 16.28 \\ 0.0025 \\ 0.0 \\ 0.0 \end{bmatrix} \tag{4}$$

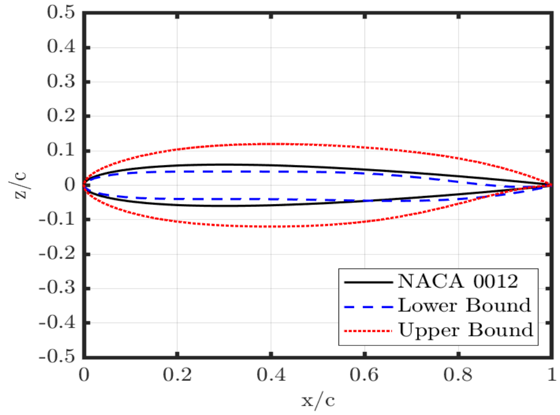

Figure 5: PARSEC upper and lower bound airfoils.

Class Shape Transformation (CST) Method The CST method, another prominent airfoil parameterization method, was introduced by Kulfan (Ref. 16). This method employs a class and shape function plus a trailing-edge thickness term to generate the upper or lower surface of an airfoil. If $\zeta = z/c$ and $\psi = x/c$ are the airfoil coordinates non-dimensionalized by chord, the equation is written as

$$\zeta(\psi) = C(\psi)S(\psi) + \psi\zeta_T, \tag{5}$$

where ζ_T is the half of the trailing edge thickness. To match the NACA 0012's trailing edge thickness for all designs, ζ_T is fixed for both the upper and lower surface to be 0.00126 in this study. $C(\psi)$ is the class function represented by

$$C(\psi) = (\psi)^{N_1}(1-\psi)^{N_2}. \tag{6}$$

N_1 and N_2 are parameters that determine how the leading and trailing edge coordinates are distributed. For example, if they are fixed values of 0.5 and 1.0 respectively, the calss function yields a rounded leading edge with a $\psi^{0.5}$ distribution and a sharp trailing edge. If $N_1 = 1.0$ and $N_2 = 0.5$, the class function would produce a sharp leading edge and a rounded trailing edge. The shape function is shown as

$$S(\psi) = \sum_{i=0}^{n} a_i K_{i,n} \psi^i (1-\psi)^{n-i}, \tag{7}$$

where $K_{i,n}$ is defined as

$$K_{i,n} \equiv \frac{n!}{i!(n-i)!}, \tag{8}$$

and a_i controls the amplitude of the basis Bernstein polynomial $K_{i,n}\psi^i(1-\psi)^{n-i}$. The parameter n denotes the order of the Berstein polynomial. In Eq. (7), an n^{th} order Bernstein polynomial generates $n+1$ curves. It is noted that the n terms on the right-hand side in Eq. (8) are different for this paper, where $n+1$ was used instead due to difficulty obtaining non-stalled airfoils with our analysis tools. This issue will be further investigated in the future with more reasonable constraints to parametric bounds.

The shape function is particularly powerful in its ability to generate complex curvatures, making the CST method very adaptable and robust. The complexity and detail of the airfoil shape can be adjusted by selecting the order of Bernstein polynomial and tuning component amplitudes. Conceptually, the parameterization is a summation of shape functions to generate a final curve used for either the upper or lower surface of an airfoil. Figure 6 shows an example of the CST outcome that reproduces the upper surface of the NACA 0012 airfoil. In the figure, component curves are generated using the value of a_i multiplied by the basis Bernstein polynomial and class functions. They are then summed with the trailing-edge thickness term to obtain the final surface or resultant curve. The amplitude a_i values are found from the least-square method for the reproduction of an NACA 0012 airfoil. The values for $n = 5$ are given below:

$$a_i = \begin{bmatrix} 0.1713 & 0.1543 & 0.1573 & 0.1403 & 0.1367 & 0.1479 \end{bmatrix}$$

Higher-order polynomials demonstrate a greater capability to accurately fit complex airfoils and provide more control of the airfoil's shape. For the optimization process utilizing the CST method, a total of 12 parameters, or $n = 5$, are employed, with six parameters dedicated to defining each of the upper and lower surfaces of the airfoil. The class function is constrained to $N_1 = 0.5$ and $N_2 = 1.0$.

The CST method parameter bounds for amplitudes a_i are,

$$\min(a_i) = \begin{bmatrix} 0.12 & 0.12 & -0.10 & 0.3 & -0.28 & 0.4 \end{bmatrix}$$
$$\max(a_i) = \begin{bmatrix} 0.35 & 0.35 & 0.35 & 0.50 & 0.35 & 0.5 \end{bmatrix}$$

These values are applied to both the upper and lower surfaces, with the lower surface adopting the opposite sign of each amplitude value. The chosen bounds are selected to encompass a broad area of the design space while avoiding configurations that would lead to airfoil surfaces crossing over or experiencing flow separation at zero angles of attack. Negative amplitudes are considered so that more complex designs are possible.

Optimization Process

The entire optimization process is illustrated in Fig. 7. The chosen methodology is surrogate model-based optimization, utilizing MATLAB's Design and Analysis of Computer Experiments (DACE) toolbox (Ref. 27). The process begins with generating airfoil geometries using Latin Hypercube sampling (Ref. 28). Subsequently, the aerodynamic and aeroacoustic performances of each rotor blade design incorporating these airfoils are evaluated. Based on the airfoil parameters and their corresponding outcomes, a surrogate model is constructed to predict the performance of unevaluated designs. This model employs Kriging interpolation to ensure it

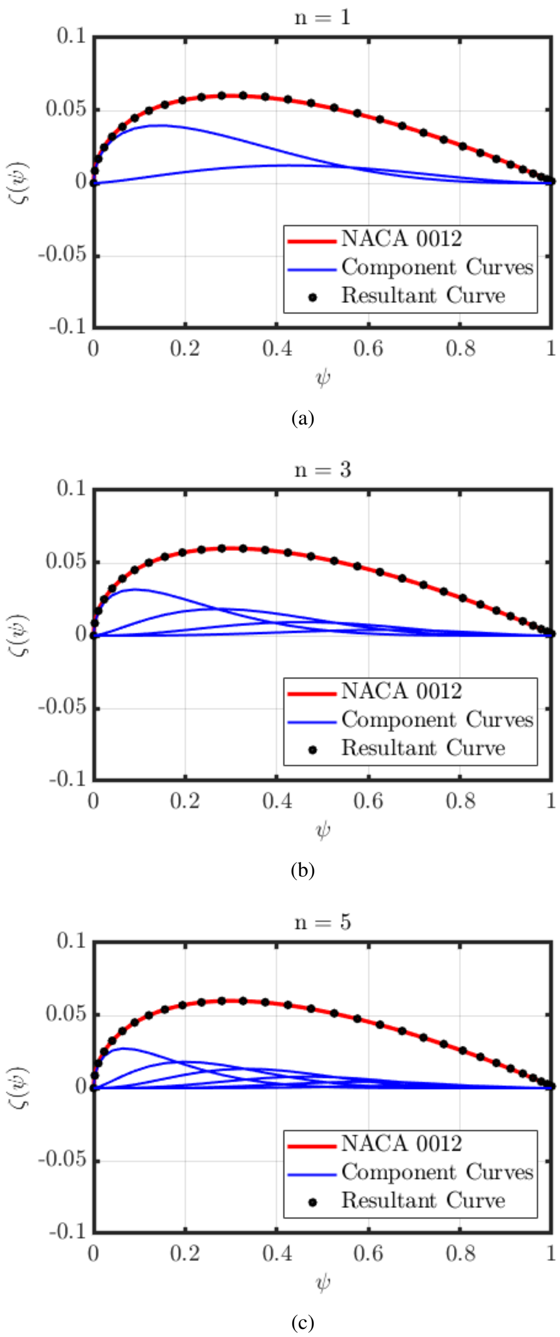

Figure 6: CST output reproducing the upper surface of the NACA 0012 airfoil using Bernstein polynomials of order: (a) n = 1, (b) n = 3, and (c) n = 5.

accurately reflects the data points (Refs. 27, 29). The mean squared error (MSE) is calculated for each design within the surrogate model. Designs exhibiting the maximum MSE are identified, and these cases are selected as additional sampling points to refine the model's accuracy. This step is iterated until the maximum MSE falls below 2%. Finally, MATLAB's built-in multi-objective genetic algorithm is used to determine optimal designs based on the surrogate model's predictions. These optimal designs are then directly assessed using BEMT and UCD-QuietFly to confirm the surrogate model's accuracy. If the average discrepancy between the surrogate's predictions and the actual results from the verification exceeds 5%, the optimization cycle is initiated again.

Kriging Interpolation The DACE MATLAB Kriging Toolbox from Lophaven, *et al.* (Ref. 27) is employed to generate a surrogate (approximate) model of the design space. This method is chosen to minimize the number of designs that need to be evaluated using UCD-QuietFly, and it follows the methodology previously demonstrated by Lee, *et al.* (Ref. 29) for the optimization of wing sails. Initially, a sample of designs comprising discrete input parameters is evaluated to determine their performance. Subsequently, a surrogate model is fitted to this data to create a continuous response surface that predicts the performance of unevaluated designs. For this study, a Kriging surrogate model is used.

The mathematical representation of the response surface is given by:

$$\hat{y}(x) = f(x)\beta^* + r(x)^T\gamma^*, \tag{9}$$

where x indicates the variable input vector of dimension n, and $\hat{y}(x)$ is the response surface's output vector of dimension q. Note that Eq. (9) is a general Kriging response surface equation and x includes any values in the user's specified range or unsampled points. The first term of the right-hand side is a linear combination of basis functions, $f(x)$, and coefficients, β^*, to fit a polynomial to the evaluated data. This linear combination is also referred to as the mean or approximate performance of the real function. This second term is the error which is approximated using statistical methods. Equation 9 can be further expanded as follows

$$f(x) = \left[\mathtt{f}_1(x), \quad \mathtt{f}_2(x), \quad \cdots, \quad \mathtt{f}_p(x)\right]^T, \tag{10}$$

$$\beta^* = (F^T R^{-1} F)^{-1} F^T R^{-1} Y, \tag{11}$$

$$\gamma^* = R^{-1}(Y - F\beta^*). \tag{12}$$

Equation 10 is a vector of $\mathtt{f}$, basis functions determined by the order polynomial selected. For this paper, the regression model uses a 0^{th} order (constant) polynomial. Thus, p and $\mathtt{f}_1(x) = 1$. The F matrix in Eq. (11) shows the design matrix, which contains the basis functions at evaluated locations s_i. Note that $s_i = S_{i,j}$ ($i = 1, \ldots, m$ and $j = 1, \ldots, n$) where m indicates the number of design sets and n is the input dimension, i.e., the number of airfoil parameters for each parameterization method in our study. ($S_{i,j}$ is the input matrix where each row is a design set and each column is an airfoil parameter.)

$$F = \begin{bmatrix} \mathtt{f}_1(s_1) & \mathtt{f}_2(s_1) & \cdots & \mathtt{f}_p(s_1) \\ \mathtt{f}_1(s_2) & \mathtt{f}_2(s_2) & \cdots & \mathtt{f}_p(s_2) \\ \vdots & \vdots & \ddots & \vdots \\ \mathtt{f}_1(s_m) & \mathtt{f}_2(s_m) & \cdots & \mathtt{f}_p(s_m) \end{bmatrix}. \tag{13}$$

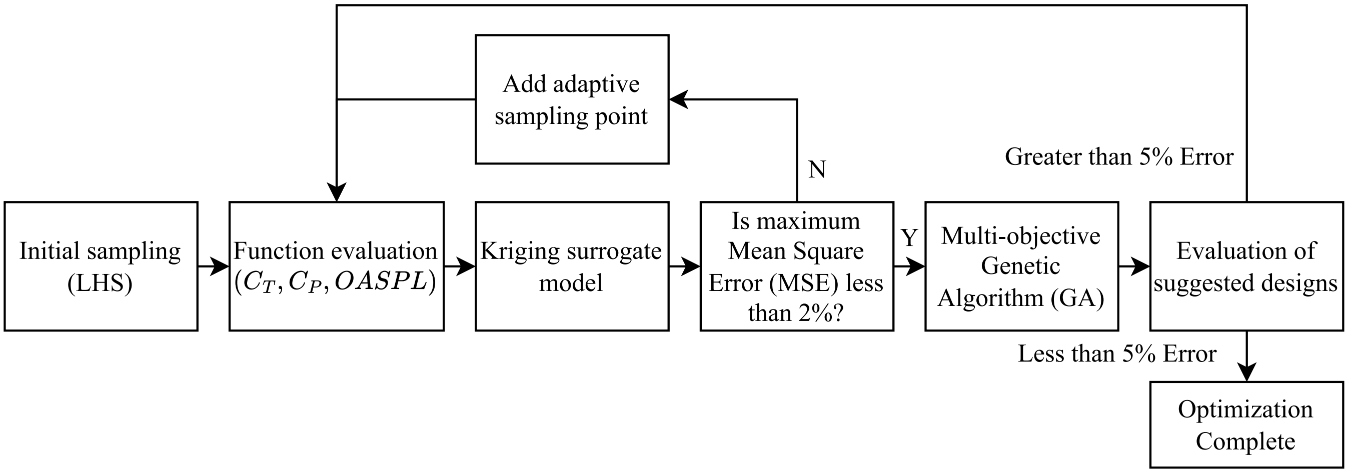

Figure 7: Optimization workflow

Note that because $p = 1$, Eq. (13) simplifies to a vector. R is an $m \times m$ matrix of spatial correlations between evaluated locations shown by,

$$R = \begin{bmatrix} \mathtt{R}(\theta, s_1, s_1) & \cdots & \mathtt{R}(\theta, s_1, s_m) \\ \vdots & \ddots & \vdots \\ \mathtt{R}(\theta, s_m, s_1) & \cdots & \mathtt{R}(\theta, s_m, s_m) \end{bmatrix}. \quad (14)$$

The correlations are modeled using the Gauss correlation function

$$\mathtt{R}(\theta, s_i, s_k) = \prod_{j=1}^{n} \exp(-\theta_j (S_{i,j} - S_{k,j})^2), \quad (15)$$

where j is the index of the design parameter such as airfoil camber, thickness, etc. The θ_j term is a parameter in the correlation model. It is solved by minimizing $|R|^{\frac{1}{m}} \sigma^2$, where $|R|$ is the determinant of R, and σ^2 is the variance. The $r(x)$ term in Eq. (9) is a vector correlating the evaluated locations s_i to variable location x including an untried point,

$$r(x) = \begin{bmatrix} \mathtt{R}(\theta, s_1, x) & \cdots & \mathtt{R}(\theta, s_m, x) \end{bmatrix}^T. \quad (16)$$

Finally, Y is an $m \times q$ matrix of observations, i.e., the results from the evaluations done by BEMT and UCD-QuietFly. Recall that q is the number of responses of interest. For this paper, $q = 3$ because we are interested in thrust, power, and A-weighted OASPL.

The initial number of evaluated points may be insufficient to create an accurate response surface. Therefore, the MSE, denoted by $\varphi(x)$, can be calculated at any given location using

$$\varphi(x) = \sigma^2 (1 + u^T (F^T R^{-1} F)^{-1} u - r(x)^T R^{-1} r(x)) \quad (17)$$

where $u = F^T R^{-1} r(x) - f(x)$. Locations with high MSE are specifically targeted for evaluation and are subsequently included to enhance the surrogate model. Figure 8 illustrates the response surface's prediction of OASPL in dBA as a function of the thickness (t) and boat-tail angle (b) parameters, while holding other parameters constant. This depiction showcases how the response surface evolves and becomes more refined as additional data points are evaluated and included. It is important to note that while the figure highlights the response for two specific parameters, similar response surfaces exist for other key factors like thrust and power, which are crucial for comprehensive rotorcraft design. The full surrogate model incorporates these and other parameters to provide a multidimensional and detailed prediction landscape.

Multi-Objective Genetic Algorithm (GA) After constructing the surrogate model, MATLAB's design and optimization toolbox offers both single and multi-objective GAs for function minimization. The function of interest derives from the response surface equation referenced as Eq. (9), which aims to maximize thrust while minimizing power consumption and OASPL in dBA. To optimize for maximum thrust, the genetic algorithm minimizes the negative value of thrust. Genetic algorithms belong to a broader class known as evolutionary optimization (EO) algorithms. These algorithms initiate with a randomly generated population, and with each iteration—or generation—the population evolves, enhancing the fitness of the solution until an optimized result is achieved. One of the key advantages of EO algorithms is that they do not require gradient information, making them particularly useful for complex or non-differentiable functions. Moreover, EOs are adept at locating the global extrema of a function, a capability supported by references (Refs. 14, 29, 30). Furthermore, multi-objective optimizations facilitated by GAs are designed to yield a set of Pareto-optimal solutions. This is especially relevant when there are multiple performance metrics to consider. In such scenarios, different designs may excel in one objective while compromising on others. The nature of EOs,

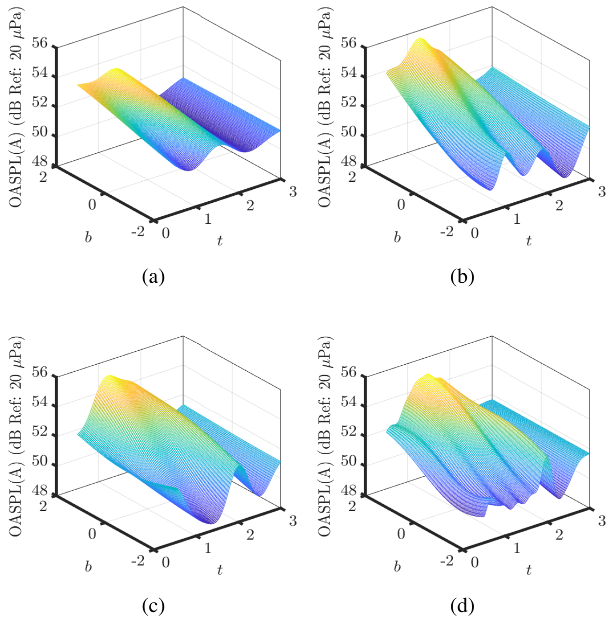

Figure 8: Surrogate response surface of OASPL(A) as a function of ParFoil's thickness (t) and boat-tail angle (b) fitted with: (a) 100, (b) 1000, (c) 5000, and (d) 10000 evaluations.

starting with a diverse population, allows for a broad exploration of the solution space, where individuals may converge to various sections of the final Pareto frontier simultaneously. This approach ensures a comprehensive search of the design space, providing a balanced set of solutions that address all objectives effectively.

In the study outlined in this paper, individuals within a population are characterized by genes that correspond to parameters defining the airfoil shape. Specifically, each generation consists of 100 individuals, and the genetic algorithm is permitted to run for 1000 generations. The initial generation is randomly generated, and the performance of each individual is evaluated using the Kriging surrogate model shown in Eq. (9). Individuals scoring above average are selected for genetic operations including crossover, mutation, and elite preservation. Crossover is implemented by selecting high-performing individuals (parents) and randomly exchanging genes to produce offspring (children) for the subsequent generation. This helps to mix and propagate beneficial traits throughout the population. Mutation involves randomly altering the genes of the offspring, introducing variability, and helping the population explore new areas of the solution space that might not be reachable by crossover alone. Elite preservation ensures that high-performing individuals from the previous generation are carried over to the next generation. This practice helps maintain high-quality traits and prevents regression in performance. The frequency of these operations is set by the user, and the cycle repeats until there is no further improvement on the Pareto frontier or other predefined stopping criteria are met. A Pareto frontier that shows no improvement is considered Pareto optimal, as depicted in Fig. 9. An individual is deemed Pareto optimal if it remains non-dominated by other points, with domination defined by two conditions: individual x_1 dominates x_2 if (1) x_1 is no worse than x_2 in all objectives, and (2) x_1 is strictly better than x_2 in at least one objective. For additional insights into multi-objective evolutionary optimizations and the specifics of genetic algorithms, readers are referred to (Ref. 30), which provides a comprehensive overview of these methodologies and their applications.

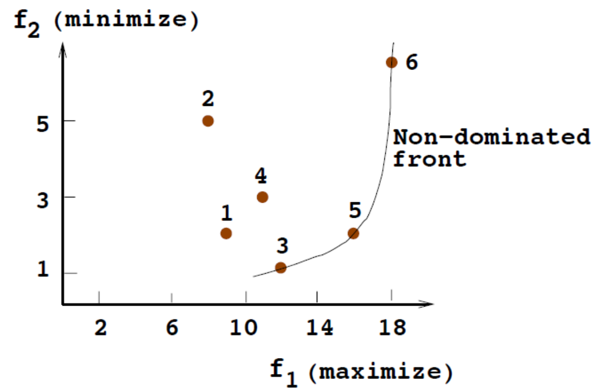

Figure 9: Example of dominated and non-dominated points (Ref. 30).

RESULTS

Ideally Twisted Rotor

The ideally twisted rotor test (Ref. 23) is employed for validating prediction tools and for conducting the airfoil optimization study. While noise reduction is a primary objective of the optimization, the Figure of Merit (FM) is also a critical metric to consider. As highlighted in (Ref. 31), even slight decreases in FM of 0.005 can reduce the passenger payload of a vehicle by 1. FM is defined as

$$FM = \frac{C_T^{3/2}}{\sqrt{2}C_P} \tag{18}$$

where C_T and C_P are the thrust and power coefficients.

The optimization results using the three airfoil parameterization methods are depicted in Fig. 10, where OASPL(A) is plotted against FM. The baseline ideally twisted rotor is marked by a red hexagram, with a FM of 0.6320 and an OASPL(A) of 57.36 dBA. There are many designs in the Pareto front that are positioned southeast of the baseline design, indicating an overall improvement characterized by a general increase in FM and a decrease in OASPL(A).

Figure 10(a) displays the design points obtained by using the ParFoil method. It is important to note, that while many points in the plot appear to be dominated in terms of OASPL(A) or FM, they are non-dominated when considering thrust and power coefficients as those are primary objectives in addition to OASPL(A). The quietest ParFoil design achieved is labeled with (a) in Fig. 10(a) and has an OASPL(A) of 53.36 dBA

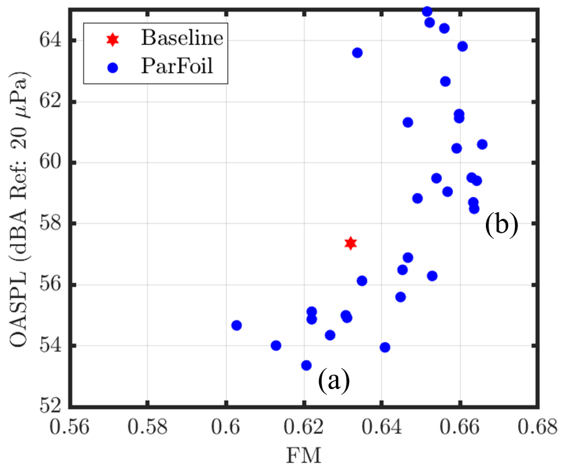

(a)

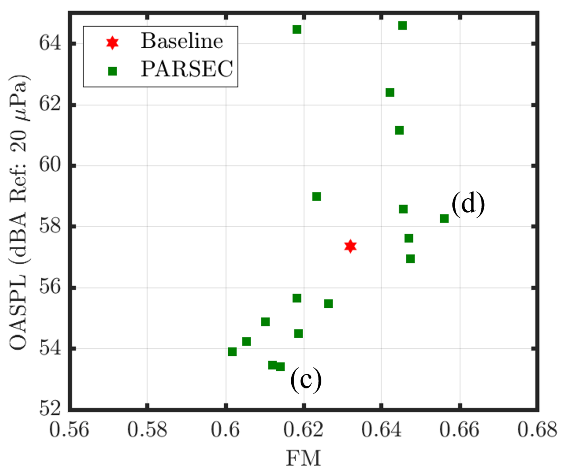

(b)

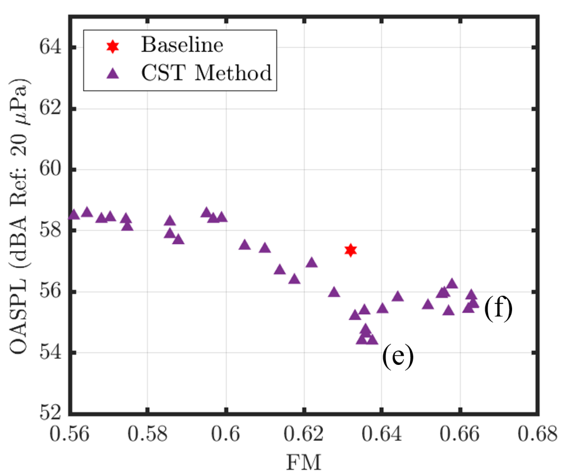

(c)

Figure 10: Optimized designs for the ideally twisted rotor: (a) ParFoil, (b) PARSEC, and (c) CST Method.

with FM of 0.6206. This represents a significant noise reduction of 4.00 dBA and a decrease in FM of 0.0114 compared to the baseline NACA 0012 design. On the other hand, the design with the highest FM labeled with (b) records an OASPL(A) of 58.49 dBA and FM of 0.6637. This indicates a noise increase of 1.13 dBA but also a substantial improvement in FM of 0.0317. Additionally, some designs balance these extremes, where one displays an OASPL(A) of 53.95 dBA and FM of 0.6408. This design shows a noise decrease of 3.41 dBA and a slight FM increase of 0.0088 from the baseline design, providing a simultaneous improvement in both noise and performance. While this study focuses on the extremes and their broadband noise characteristics, this optimization methodology does produce designs that are objectively better with few trade-offs.

Figure 10(b) displays the results obtained using the PARSEC parameterization method. The Pareto front obtained through PARSEC is similar to that of ParFoil, though it appears to be slightly less optimal. The quietest design achieved with PARSEC labeled with (c) reaches an OASPL(A) of 53.41 dBA with FM of 0.6140. This represents a reduction of 3.95 dBA in noise and a decrease of 0.0180 in FM. The design labeled (d) has the highest FM of all the PARSEC designs and demonstrates a modest noise reduction, with a decrease in OASPL(A) of 0.41 dBA and an increase in FM of 0.0150. The reasons behind these differences compared to ParFoil results are analyzed and discussed later in this section.

Finally, Fig. 10(c) displays the results from the CST method. The optimized result depicted is markedly different from the expected pattern, as it includes many more designs with low FM. The low FM is primarily due to flow separation with thick airfoils. While such configurations may maximize thrust, the accompanying increase in drag and power significantly reduces FM. Additionally, flow separation is not desirable for noise, leading to the dismissal of these designs from further consideration. The quietest design labeled with (e) obtained through the CST method achieves a reduction of 3.06 dBA in OASPL(A) with a slight increase in FM of 0.0055. The design with the highest FM labeled with (f) shows a decrease of 1.75 dBA in OASPL(A) and an increase of 0.0310 in FM. Therefore, despite numerous designs appearing west of the baseline, indicating poorer performance, the optimization process still yields airfoils with commendable performance improvement and noise reduction.

For each parameterization method, the airfoils that resulted in the quietest and highest FM design are illustrated in Fig. 11 and follow the same labeling previously used in this section (a-f). Additionally, Table 2 provides detailed performance metrics for these designs, including thrust, power, FM, and OASPL(A). This comprehensive presentation allows for a direct comparison of how different airfoil shapes influence overall performance and acoustic properties, showcasing the effectiveness of each parameterization method in achieving optimal aerodynamic and aeroacoustic outcomes.

All the parameterization methods exhibit similar performance in terms of FM and OASPL(A). Figure 12 displays the Pareto

Table 2: Performance of various designs for the optimized ideally twisted rotor

Design	**Thrust Coefficient (C_T)**	**Power Coefficient (C_P)**	**FM**	**OASPL (dBA)**
Baseline	1.382×10^{-2}	1.818×10^{-3}	0.6320	57.36
ParFoil (a)	1.382×10^{-2} (+0.00%)	1.851×10^{-3} (+1.82%)	0.6206 (−1.80%)	53.36 (−4.00)
ParFoil (b)	1.622×10^{-2} (+17.37%)	2.201×10^{-3} (+21.07%)	0.6637(+5.02%)	58.49 (+1.13)
PARSEC (c)	1.376×10^{-2} (−0.43%)	1.859×10^{-3} (+2.26%)	0.6140 (−2.85%)	53.41 (3.95)
PARSEC (d)	2.024×10^{-2} (+46.45%)	3.145×10^{-3} (+72.99%)	0.6474 (+2.44%)	56.95 (−0.41)
CST (e)	1.481×10^{-2} (+7.16%)	1.999×10^{-3} (+9.96%)	0.6375 (−0.87%)	54.39 (−2.97)
CST (f)	1.716×10^{-2} (+24.17%)	2.396×10^{-3} (+31.79%)	0.6634 (+4.97%)	55.61 (−1.75)

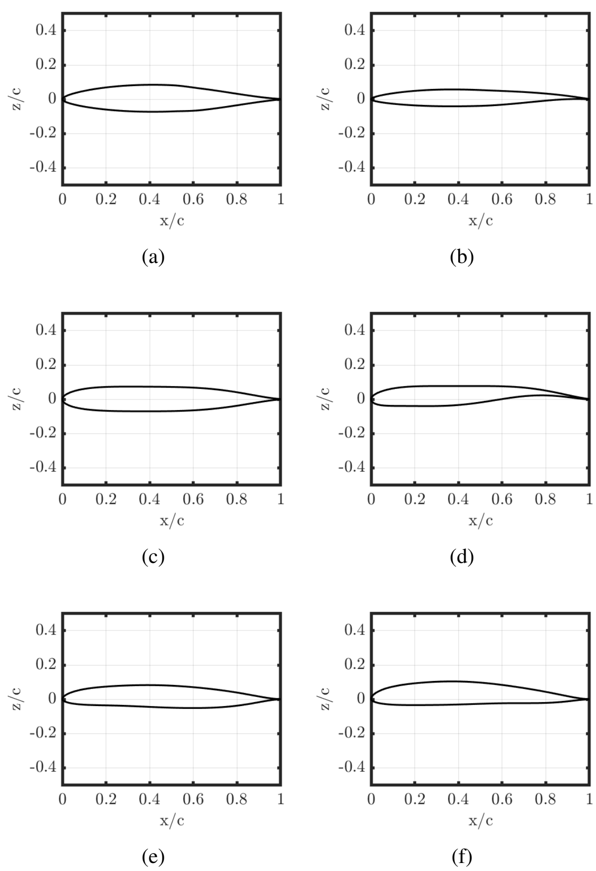

Figure 11: Optimized airfoils for quietest design (left) and highest FM design (right) for: (a, b) ParFoil, (c, d) PARSEC, and (e, f) CST.

fronts of each airfoil parameterization plotted against each other. They appear to converge to a general area, achieving a maximum FM of approximately 0.66 and a minimum OASPL(A) of 53 dBA. This convergence may suggest that performance improvements might plateau with the current optimization focusing only on the $r/R = 0.7 - 1.0$ region. However, additional cases and further analysis are necessary to confirm this hypothesis and determine if broader optimizations could yield significantly better results.

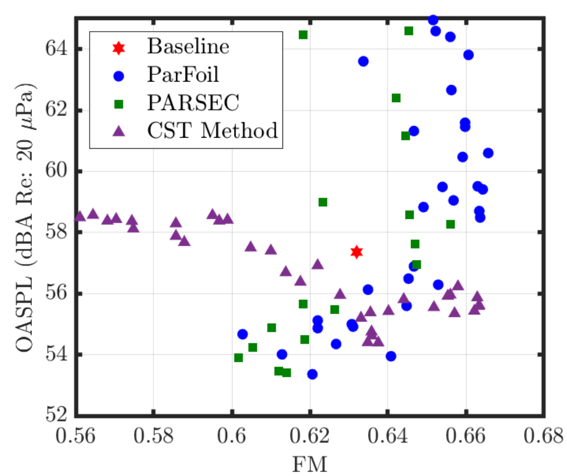

Figure 12: Comparison of optimized performance of each parameterization method.

Figure 13 displays the quietest airfoils from the ParFoil, PARSEC, and CST methods plotted against each other. Both ParFoil and PARSEC's quietest airfoils demonstrate very similar characteristics, particularly in terms of overall thickness and the configuration of their trailing edge sections, which largely overlap. This similarity is likely the reason both designs achieved a 4.0 dBA decrease in noise. However, the PARSEC airfoil exhibits less camber compared to the ParFoil-optimized airfoil, which accounts for its lower FM. The reason PARSEC does not converge to the same slightly cambered profile as ParFoil may be attributed to the parameter bounds set during the optimization process. A fundamental distinction between ParFoil and PARSEC lies in their approaches: ParFoil modifies features of an existing airfoil, whereas PARSEC directly alters the upper or lower surface through a polynomial function. Referring to Eqs. (1)–(3), small shape changes localized to specific sections of the polynomial might necessitate large adjustments to the combination of parametric values, which may exceed the user-defined bounds. Expanding these bounds was not considered a viable solution, as it could lead to a greater number of invalid designs, such as instances where an airfoil's upper surface might cross below the lower surface or vice versa. Since the surrogate model is fitted to sampled data, introducing invalid parameter combinations could result in high uncertainty regions within the response surface, complicating the model's predictive accuracy and utility. This limitation underscores the importance of carefully setting and evaluating the bounds and parameters within each optimization methodology to achieve both valid and optimized airfoil designs.

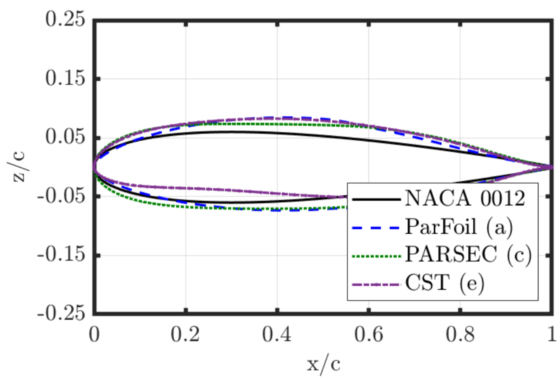

Figure 13: Optimized airfoils that yield the lowest OASPL(A) for each parameterization method.

The quietest airfoil identified through the CST method exhibits notable differences compared to those optimized using ParFoil and PARSEC for the lower surface, where it is much thinner in the first half of the airfoil but gets thicker in the rear half. This reduced thickness in the CST airfoil's lower surface likely contributes to a decreased FM loss—about 1% compared to the approximately 2% observed with the other methods. However, OASPL(A) for the CST-optimized airfoil is approximately 1 dBA higher than those optimized by ParFoil or PARSEC. Something interesting about this airfoil's upper surface is for the regions where the ParFoil airfoil disagrees with PARSEC, it has the same z/c values of PARSEC and vice versa. The shape near the trailing edge for all airfoils is similar for all three airfoils which likely contributes to why these airfoils are the quietest designs obtained.

Figure 14 shows the optimized airfoils with the highest FM from each parameterization method. The fact that each method converged on very different airfoil designs again suggests that the parameter bounds set for these optimizations might have been too restrictive, potentially limiting the exploration of the full design space. The ParFoil (b) and CST (f) designs have approximately the same FM but appear to achieve this performance through different approaches. ParFoil (b) is thinner than the NACA 0012 and is slightly cambered towards the trailing edge which explains the low power and greater thrust needed to increase FM. The CST (f) design is surprisingly thin, only having a thickness of 12% chord length. However, most of its thickness is in the upper surface yielding a highly cambered airfoil that obtains a 24.17% increase in thrust. The PARSEC (d) airfoil did not improve FM as much as the other two methods. However, the features of this airfoil are similar to the ParFoil (b), where it has increased camber in the aft regions of the chord.

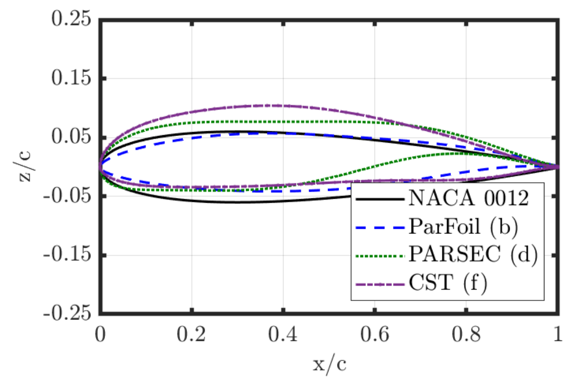

Figure 14: Optimized airfoils that yield the highest FM for each parameterization method.

Figure 15 illustrates the trailing-edge noise sound spectra results for the ideally twisted rotor, where baseline prediction aligns closely with the measured data. In this comparison, the baseline blade noise is contrasted with that of the quietest designs from each parameterization method. The CST (e) blade exhibits a notably higher sound pressure level compared to those from the ParFoil (a) and PARSEC (c) designs. However, it is important to note that its thrust coefficient is also higher by 6.68%. A higher thrust coefficient allows for a lower rotation rate to achieve the same dimensional thrust. Given that the velocity experienced by each blade section is a major contributor to trailing-edge noise, the reduction in rotation rate enabled by a higher thrust coefficient can potentially further reduce noise levels.

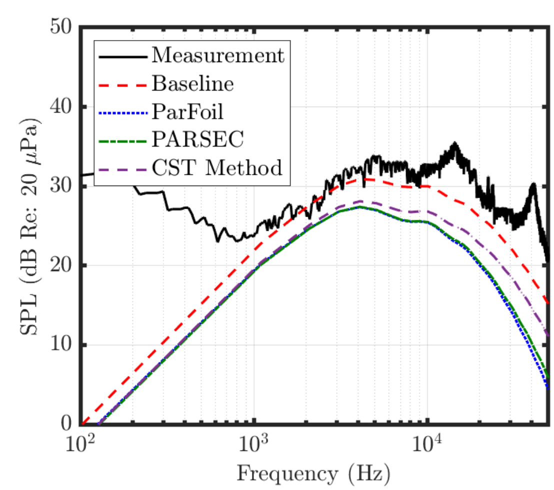

Figure 15: Ideally twisted rotor trailing-edge noise sound spectra for the baseline and optimized blades compared with experimental data (Ref. 23).

The rotation rate can be adjusted using the following equation:

$$\Omega_1 = \Omega_0 \sqrt{\frac{C_{T_0}}{C_{T_1}}}, \tag{19}$$

where the subscripts 0 and 1 denote the original and new conditions, respectively. Notice that the CST Method (f) in table 2 achieved a 24% increase in thrust and a 4.97% increase in figure of merit while decreasing OASPL(A) by 1.75 dBA relative to the baseline. A comparison between CST-optimized blades is shown in the sound spectra provided by Fig. 16. A 24% increase in thrust allows a 10% decrease in rotation rate from approximately 5500 to 4930 RPM. The resulting OASPL(A) of design (f) with a reduced rotation rate is 53.41 dBA, which is 2.2 dBA less than (f) and 1 dBA less than design (e) operating at the 5500 RPM. Therefore, significantly higher thrust coefficients can lead to high FM designs that are more performant acoustically than blades that are optimized with noise as the only objective if rotation rate is considered.

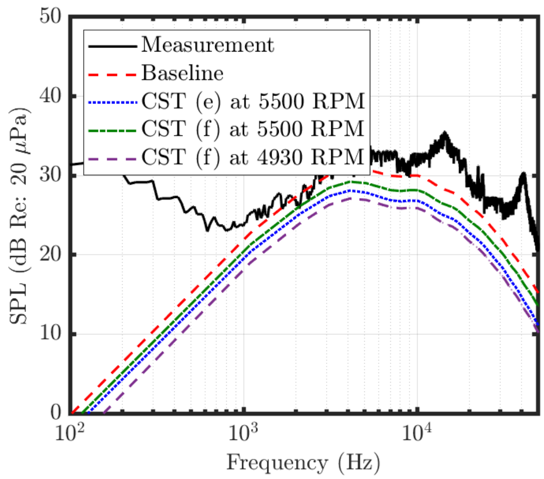

Figure 16: Ideally twisted rotor trailing-edge noise sound spectra for the baseline and CST-optimized blades at different rotation rates (Ref. 23).

The radial distribution of OASPL(A) for the quietest designs obtained by each method for the baseline 5500 RPM is illustrated in Fig. 17. A discontinuity at the $r/R = 0.7$ location results from modeling the blade using constant airfoils without interpolating between the inboard and outboard sections. This figure aligns with expectations: both ParFoil (a) and PARSEC (c) yielded similar airfoils and acoustic performance, whereas the CST method's design is slightly louder than the others but still quieter than the baseline at the tip section.

Boundary layer parameters, crucial for the wall pressure spectrum model, vary significantly with radius. These parameters are taken from the $x/c = 0.99$ location on each radial section. Figure 18 illustrates the displacement thickness of the boundary layer across the blade radius. It is observed that the optimized airfoils demonstrate a higher displacement thickness compared to the baseline case. Interestingly, the magnitude order among the optimized blades does not correlate with their respective OASPL(A), as shown in Fig. 17. A similar observation applies to the boundary layer thickness and

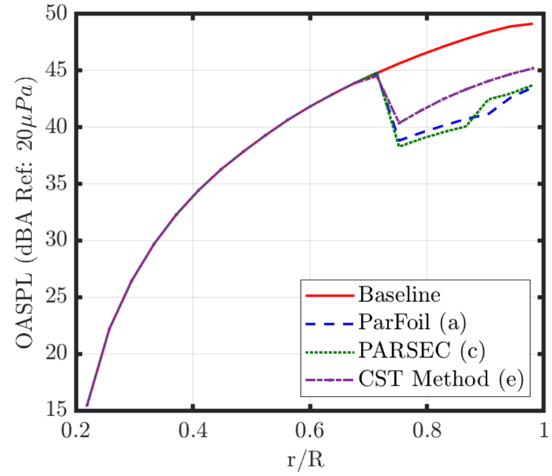

Figure 17: Radial distribution of OASPL(A) of each blade section for the baseline and quietest designs from each parameterization method.

momentum thickness, although these are not detailed in the paper. This suggests that the boundary layer thickness, displacement thickness, and momentum thickness may not be the primary factors driving noise reduction.

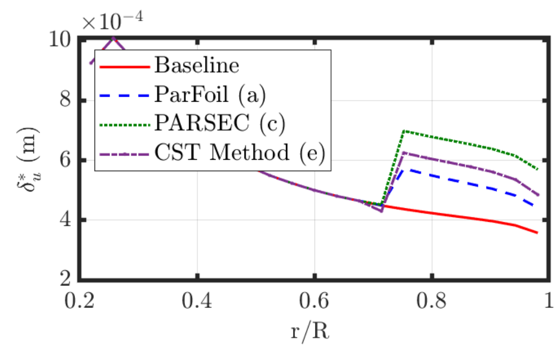

(a)

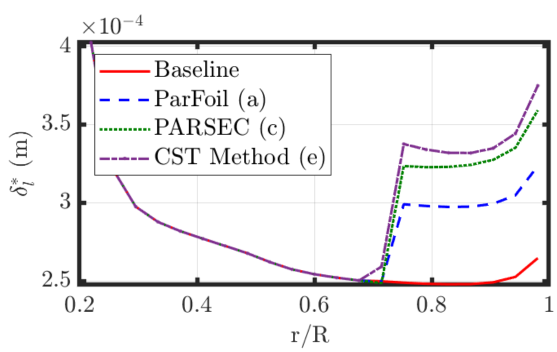

(b)

Figure 18: Radial distribution of boundary layer displacement thickness near the trailing edge: (a) suction side and (b) pressure side.

Consequently, the reduction in OASPL(A) can primarily be attributed to other boundary layer parameters, specifically the chordwise pressure gradient and the friction coefficient. Figure 19 displays the pressure gradient across the blade radial locations, presented in terms of absolute value. This approach is adopted since Lee's wall pressure spectrum model (Ref. 7) uses the absolute value of the pressure gradient. The friction coefficient is depicted in Fig. 20. Although all optimized designs exhibit increased boundary layer, displacement, and momentum thicknesses, they also feature significantly lower friction coefficients and pressure gradients at the trailing edge, which appear to substantially mitigate OASPL(A). In Lee's wall pressure spectrum model (Ref. 7), the friction coefficient—or wall shear stress—plays a crucial role, influencing two specific terms: the amplitude correction and the non-dimensional pressure gradient, also known as the Clauser parameter. When the wall shear stress decreases, the amplitude correction term decreases, but the Clauser parameter increases. Typically, apart from exceptionally high values of the Clauser parameter, the wall pressure spectrum tends to decrease as the shear stress decreases. Physically, the pronounced energy and momentum exchange within the turbulent layers is represented as higher shear stress. The pressure gradient is also a determinant factor for the Clauser parameter; as this value decreases, the wall pressure spectrum decreases correspondingly. In traditional airfoils, such as with NACA airfoils, at varying angles of attack, the boundary layer thickness and pressure gradient can exhibit similar trends. However, in scenarios where these parameters diverge in behavior, the pressure gradient or wall shear stress generally predominates, overshadowing the influence of the boundary layer thickness. This phenomenon occurs because the pressure gradient directly impacts the flow unsteadiness and the potential for flow separation, which are critical factors in aerodynamic noise generation. When there is a strong pressure gradient or high wall shear stress, these forces can significantly modify the flow characteristics, sometimes countering the effects observed due to changes in the boundary layer thickness. More specifically in Figs. 19 and 20, on the suction side, all the optimized blades exhibit a significantly reduced pressure gradient and skin friction near the blade tip. Conversely, on the pressure side, the CST method displays behavior similar to the baseline for the pressure gradient, while the other two methods, ParFoil and PARSEC, show a substantially lower pressure gradient. This observation corresponds well with OASPL(A) results, as illustrated in Fig. 17.

Finally, despite the thin airfoils and low angle of attack at the tip, which generally reduce the likelihood of flow separation, it remains crucial to verify whether the airfoils are experiencing separation, as Lee's wall pressure spectrum model does not apply to highly separated flows. Figures 21 and 22 depict the chordwise distribution of pressure and friction coefficients at $r/R = 0.95$. The pressure distribution for all optimized designs remains relatively flat beyond $x/c = 0.90$, a trend clearly visible when comparing these results to those of the baseline NACA 0012, or the reduced pressure gradient as illustrated in Fig. 19. Additionally, the friction coefficient plot indicates relatively low, and importantly, non-negative values for the optimized designs, suggesting that the flow remains attached and confirming the applicability of the model used.

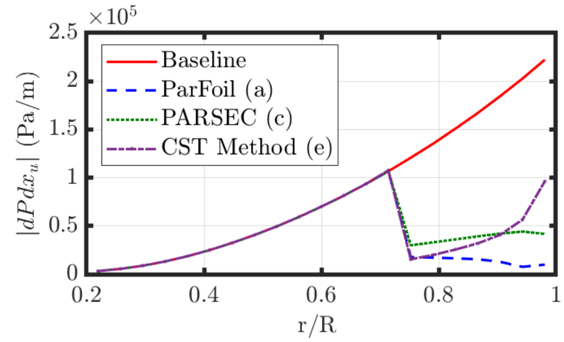

(a)

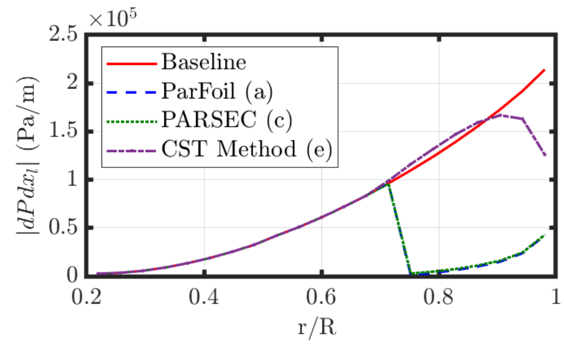

(b)

Figure 19: Radial distribution of chordwise pressure gradient near the trailing edge: (a) suction side and (b) pressure side.

XV-15 Hover

Figure 23(a) presents comparisons of FM as a function of the thrust coefficient (C_T) between experimental data and predictions for both the full blade and the truncated (shortened) blade. The blade is shortened to reduce the tip Mach number by half from the original full blade. The experimental data indicate a maximum FM of about 0.78 at a C_T value of 0.0105. Predictions for the full blade show a maximum FM of approximately 0.8 at a C_T value of 0.011, while the shortened blade displays a maximum FM of about 0.76 at the same C_T value. At higher values of C_T, FM decreases due to stall. At lower C_T values, the full blade predictions align well with the experimental data, whereas the shortened blade underpredicts FM. This discrepancy may be attributed to a different Mach number and Reynolds number between the shortened airfoil and the measurement. However, overall, the predictions are reasonable when compared with the experimental data. Optimization is conducted on the shortened blade at two blade sections ($r/R = 0.7-0.9$ and $0.9-1.0$) at its highest FM configuration, which features a collective pitch angle of 14.0 degrees and a thrust coefficient and FM of 0.0114 and 0.7585, respectively. Figure 23(b) shows the optimization results using the ParFoil method, employing the same parameters selected for the ideally twisted rotor optimization. The baseline blade predicts OASPL(A) of 52.08 dBA. The quietest design achieves a reduction of 3.47 dBA in noise levels, but it also resulted in a decrease of 0.0047 in the FM, yielding an OASPL(A) and FM of 48.61 dBA and 0.7538, respectively.

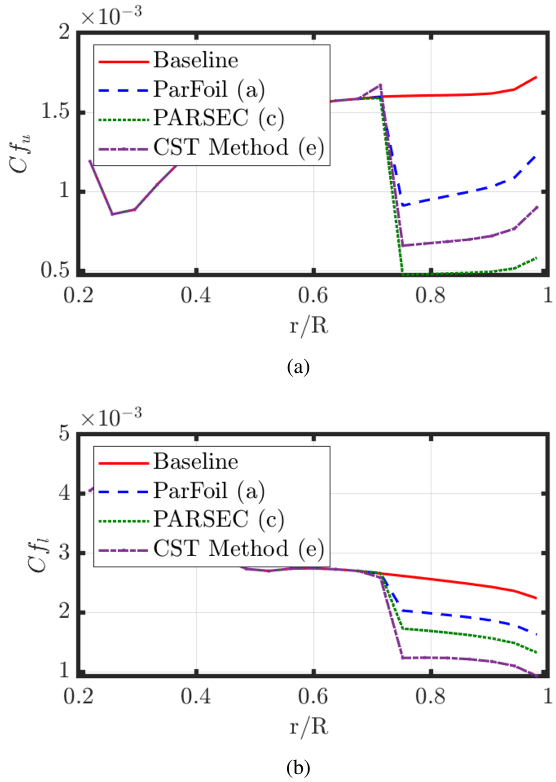

Figure 20: Radial distribution of friction coefficient near the trailing edge: (a) suction side and (b) pressure side.

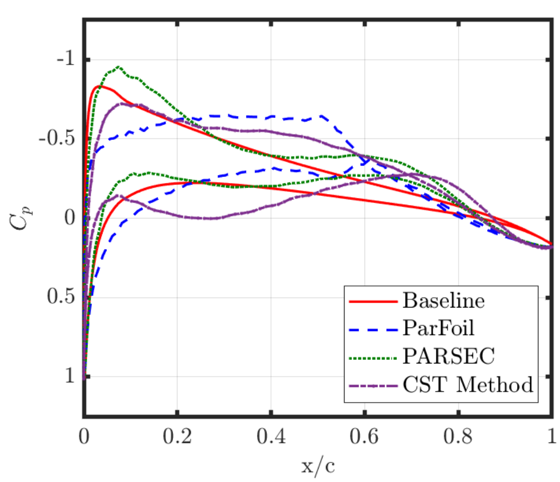

Figure 21: Chordwise pressure coefficient distribution at $r/R = 0.95$

The airfoils depicted in Fig. 24 illustrate the baseline and optimized airfoil shapes at the $r/R = 0.7-0.9$ and $0.9-1.0$ sections, and Table 3 presents the ParFoil parametric values with respect to corresponding baseline airfoils, including camber scaling factor (m), camber crest location (p_0), thickness scaling factor (t), trailing-edge camber (n), trailing-edge camber crest location (q_0), boat-tail angle factor (b), and leading-edge radius scaling factor (k). For the detailed equations for the parameters, readers can refer to reference (Ref. 10). The interplay of these parameters modifies the airfoil surface in a complex manner. For instance, despite a scaling parameter for the leading edge that is less than 1.0, the resulting leading-edge radius for the modified NACA64-(1.5)12 shown in Fig 24(a) appears to increase, due to the maximum thickness shifting forwards. Another notable characteristic of this airfoil design is the introduction of negative camber at the trailing-edge region. This modification is consistent with findings from research by Liu and Lee (Ref. 10), where the integration of Lee's wall pressure spectrum model with Howe's trailing-edge noise model (Ref. 13) demonstrated that negative camber at the trailing edge of a NACA 0012 airfoil can effectively reduce noise levels. This approach was recently validated by Kang and Lee (Ref. 32) through large eddy simulations that confirmed noise reduction at the trailing edge with the application of negative camber. Overall, at $r/R = 0.7-0.9$, the optimized airfoil becomes more symmetric; the position of maximum thickness shifts toward the leading edge compared to the baseline airfoil; and the trailing-edge camber is negative. At $0.9-1.0$, the airfoil becomes thinner and features a higher trailing-edge camber.

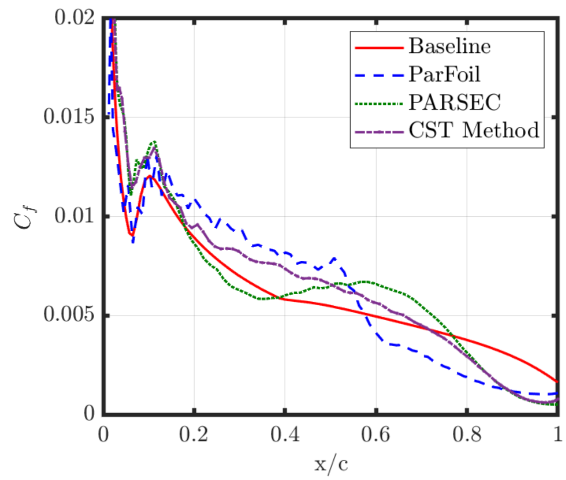

Figure 22: Chordwise friction coefficient distribution for the suction side at $r/R = 0.95$

A comparison of the one-third octave band sound spectra of trailing-edge noise is illustrated in Fig. 25. Since there are no experimental results available for comparison, the analysis only involves a comparison between the baseline-shortened XV-15 blade and the optimized version. Notably, there is a significant decrease in the sound pressure level across all frequencies. The primary reason for the noise reduction is the same as the ideally twisted rotor: the decrease in the pressure gradient. Figure 26 displays the spanwise distribution of the magnitude of the pressure gradient on the suction side, where the new airfoils at the tip sections exhibit a significantly lower pressure gradient compared to the baseline airfoils.

XV-15 Axial Flight

The evaluation of the XV-15 optimization blades for hover extends into axial flight conditions, specifically vertical take-off or climb mode, rather than conducting a separate optimiza-

Table 3: ParFoil parameters for quietest XV-15 optimized design with respect to corresponding baseline airfoils.

Baseline Airfoil	m	p_0	t	n	q_0	b	k
NACA64-(1.5)12	0.6769	0.3316	1.062	-0.0025	0.6567	1.428	0.8305
NACA64-208	1.3383	0.3883	0.895	0.0042	0.8668	1.566	1.3287

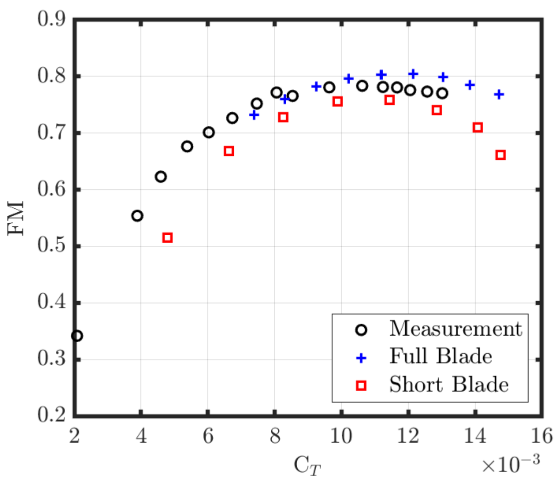

(a)

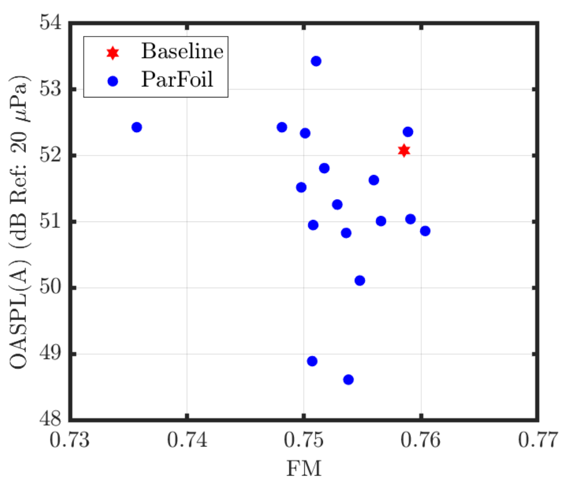

(b)

Figure 23: XV-15 blade results: (a) FM versus thrust coefficient and (b) optimized design for a shortened blade

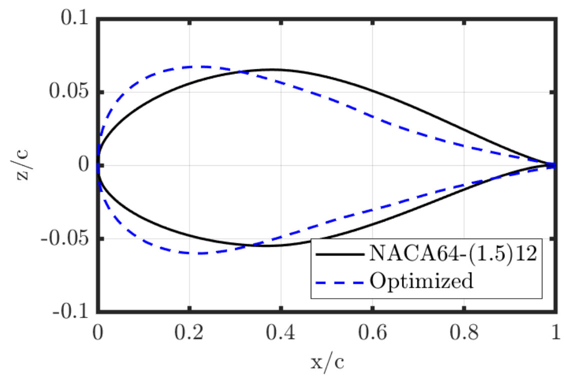

(a)

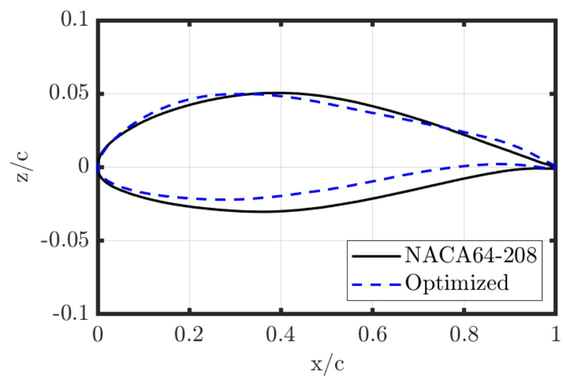

(b)

Figure 24: Comparison of baseline XV-15 airfoils to optimized airfoils: (a) $r/R = 0.7-0.9$ and (b) $0.9-1.0$.

tion for axial flight. This approach is taken because, although a tilt-rotor design for UAM is predominantly expected to operate in propeller mode (cruise) for the majority of its operational time, vertical climb and hover phases are anticipated to generate more significant broadband noise on the ground due to the noise directivity and the proximity of the source to the observer. Broadband noise is most intense normal to the rotor plane, resulting in reduced noise impact for ground observers when the rotor is in propeller mode. Additionally, both hover and vertical climb occur closer to the ground compared to cruise, heightening their noise implications. The axial velocities analyzed include 0.0 m/s (hover), as well as 5.0, 10.0, and 20.0 m/s. For consistency, the observer locations are maintained at a constant distance of 40R from the center of the rotor across all scenarios. The rotor's rotation rate is kept steady at 582 RPM in each case. However, to maintain consistent thrust across different flight modes, the collective pitch angle is adjusted. This adjustment is necessary because the sectional effective angle of attack decreases with increasing axial velocity, which results in a reduction in thrust. The use of collective pitch to match thrust is critical because altering the rotation rate to achieve the same dimensional thrust would result in significantly different Mach and Reynolds numbers, changing the noise characteristics. For instance, in the 20.0 m/s case with a baseline collective pitch of 14 degrees, the thrust coefficient (C_T) is 0.001308, which is approximately 8.7 times lower than the hover C_T. To achieve equivalent di-

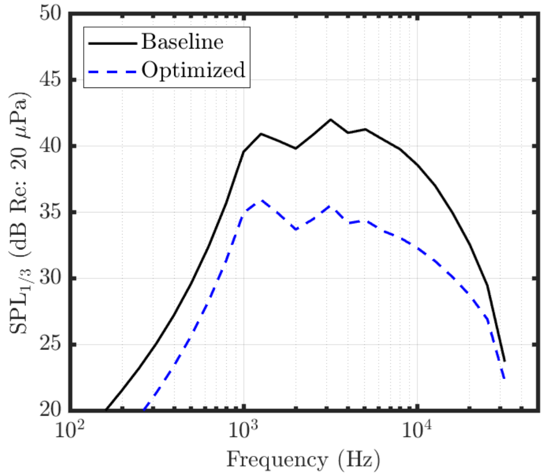

Figure 25: One-third octave band sound spectra comparing the baseline rotor to the optimized rotor.

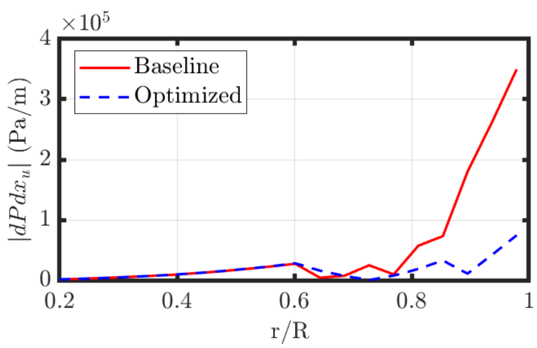

Figure 26: Radial distribution of chordwise pressure gradient at the trailing edge on the suction side for the baseline rotor and the optimized XV-15 blade.

mensional thrust at this pitch angle, the rotor would require roughly triple the rotation rate, which may not be possible or realistic.

Figure 27 displays a directivity of OASPL(A) for the baseline shortened XV-15 blade, where 90° corresponds to a position normal to the rotor plane: directly above for vertical climb. The OASPL(A) trends show an increase in noise with axial velocity at locations downstream of the rotor, while there is a slight decrease upstream of the rotor. The difference in OASPL(A) for the $V_c = 20.0$ m/s case at the 270° observer location compared to the hover case is 1.36 dBA. This modest increase in noise with axial velocity can be attributed to the increase in freestream velocity that each blade section experiences. However, because the rotation rate results in a much higher tangential velocity at each blade section compared to the axial velocity, the differences in noise levels between the 0.0 m/s and 20.0 m/s axial flows are not markedly significant. This indicates that while axial velocity impacts the noise output, the predominant noise-producing factor remains the blade's tangential motion, which far exceeds the effects of the axial flow under these operational conditions.

The OASPL(A) directivity results comparing the optimized design to the baseline are illustrated in Figs. 28–30 for axial

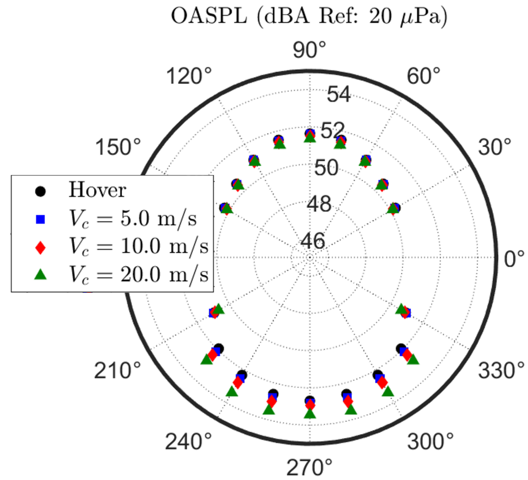

Figure 27: Directivity pattern of OASAPL(A) for the baseline rotor at various axial velocities (V_c).

velocities of 5.0, 10.0, and 20.0 m/s, respectively. The optimized rotor exhibits noise reductions ranging from 3 dBA to 5 dBA depending on the observer location. Table 4 details the noise reduction in OASPL(A) compared to the baseline at the 270° observer location, demonstrating reductions of about 3.5 - 4.3 dBA. This consistent level of noise reduction across different speeds can be attributed to the similar Reynolds and Mach numbers experienced by each blade section, coupled with the matching of the thrust coefficient. This trend is clearly shown in the distribution of effective angle of attack in Fig. 31, where the tip sections maintain a similar effective angle of attack across different flight conditions. As these sections operate under similar Reynolds and Mach numbers, the boundary layer characteristics remain consistent. However, slight variations in the freestream velocity may induce slightly different edge velocities. In sum, the airfoils optimized for hover conditions are effective in vertical climb, demonstrating their adaptability across various operational modes.

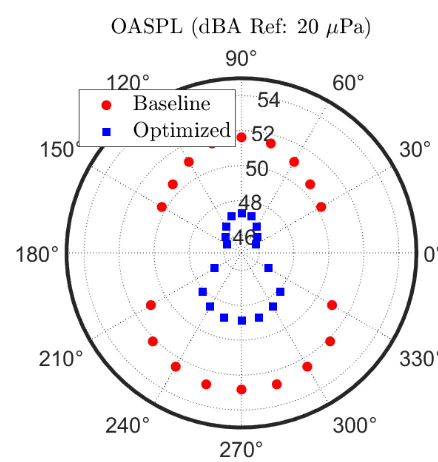

Figure 28: Noise directivity for XV-15 rotor in axial flight with $V_c = 5.0$ m/s.

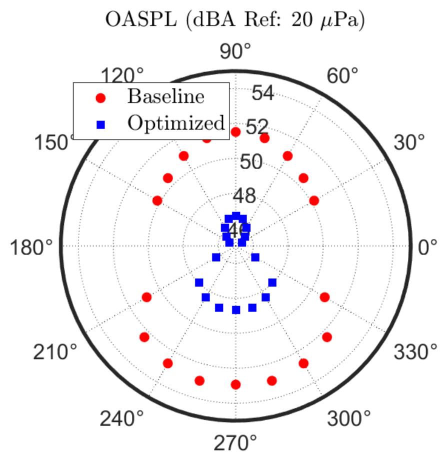

Figure 29: Noise directivity for XV-15 rotor in axial flight with $V_c = 10.0$ m/s.

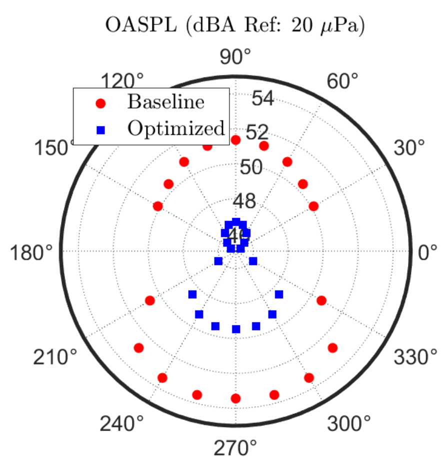

Figure 30: Noise directivity for XV-15 rotor in axial flight with $V_c = 20.0$ m/s.

CONCLUSION

Optimization was performed using a multi-objective genetic algorithm paired with a Kriging surrogate model to enhance thrust, power, and OASPL(A) for an ideally twisted rotor and a truncated XV-15 blade. The focus was particularly on the tip sections due to their critical role in aerodynamics and noise characteristics. The comparative analysis involved three parameterization methods: ParFoil, PARSEC, and the CST method, to determine which method offers the best results for optimizing these three objectives. The results indicated that all three methods yielded similar performance when generating Pareto optimal sets. The optimized performance curves for OASPL(A) and FM show a potential decrease of up to 4 dBA and an increase of up to 0.03 in FM. Although the overall performance curves converged to similar regions for each parameterization method, the individual airfoils demonstrating the highest performance for each method exhibited varying shapes. Notably, the quietest design achieved by the CST method was approximately 1 dBA louder than those achieved by PARSEC and ParFoil. A closer examination of the airfoil shapes revealed that ParFoil and PARSEC produced similar airfoils in terms of thickness and boat-tail angles, whereas the CST method resulted in a thinner airfoil with significantly more camber. This discrepancy in optimized geometries could potentially stem from insufficiently defined parametric value bounds. Thus, more attention is needed in bounding these values such that each method covers the same design space without generating invalid designs such as non-physical airfoils or airfoils with flow separation.

Table 4: Noise reduction of the optimized XV-15 compared to the baseline rotor at the 270° observer location.

Axial Velocity (m/s)	**Δ OASPL(A) (dB)**
0.0	−3.47
5.0	−3.95
10.0	−4.27
20.0	−3.85

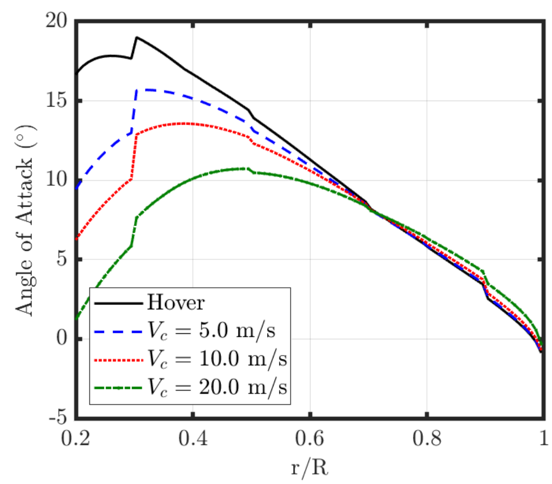

Figure 31: Radial distribution of effective angle of attack for various flight conditions.

Despite the differences in optimized geometries among the parameterization methods, they all effectively reduced trailing-edge noise through consistent boundary layer characteristics, particularly the reduced chordwise pressure gradient and the friction coefficient near the trailing edge. The quietest designs across all methods successfully achieved lower OASPL(A) values by reducing these factors, even though there was an increase in the boundary layer, displacement, and momentum thickness.

The effectiveness of the hover optimization was demonstrated in the XV-15 hover tests using the ParFoil method, where a significant reduction in the OASPL(A) by 3.47 dBA was observed. This reduction was primarily attributed to the decrease in the chordwise pressure gradient in the optimized airfoils compared to the baseline geometries. Further evaluation of these optimized airfoils was conducted under axial flight conditions, showcasing the versatility and robustness of the hover-optimized designs. In axial flight, the introduction of an axial velocity component naturally reduces the effective angle of attack. To compensate for this reduction and maintain performance, an increase in collective pitch was implemented instead of adjusting the rotation rate. This strategic adjustment allowed the hover-optimized tip section airfoils to operate efficiently at similar Reynolds and Mach numbers across different axial velocities while sustaining the same thrust levels as in the hover case. The performance of these optimized airfoils under varied axial velocities consistently showed a decrease in OASPL(A) ranging from approximately 3.5 to 4.3 dBA when compared to the baseline XV-15 blade. This success indicates that optimizations aimed at reducing specific aerodynamic parameters, such as the chordwise pressure gradient during hover, can yield beneficial outcomes that extend beyond the initial conditions.

While this study has made significant strides in utilizing low-fidelity tools for the acoustic validation of optimized airfoils, further research is imperative to fully ascertain and enhance the effectiveness of these methodologies. Although the theoretical underpinnings, such as the impact of reducing the pressure gradient on minimizing the wall pressure spectrum, are well understood and supported by prior studies, the current aerodynamic and acoustic models employed are still categorized as low-fidelity. To bridge the gap between theoretical predictions and practical applications, future investigations should incorporate high-fidelity simulations, such as large eddy simulations, or experimental approaches to directly measure the wall pressure spectrum and associated noise. These advanced methodologies would provide a more detailed and accurate validation of the optimization techniques developed, confirming their utility and effectiveness in real-world scenarios. Additionally, exploring variations in geometric parameters such as twist and chord length presents another promising avenue for research. Adjustments in these aspects of blade design have the potential to significantly influence acoustic performance, offering further opportunities for optimization and refinement.

ACKNOWLEDGMENTS

The authors appreciate the financial support from Supernal for UAM broadband noise research.

REFERENCES

1. Sarojini, D., Ruh, M., Joshy, A., Yan, J., Ivanov, A., Scotzniovsky, L., Fletcher, A., Orndorff, N., Sperry, M., Gandarillas, V., Asher, I., Chambers, J., Gill, H., Lee, S., Cheng, Z., Rodrigues, G., Zhao, S., Mi, C., Nascenzi, T., Cuatt, T., Winter, T., Guibert, A., Cronk, A., Kim, H., Meng, S., and Hwang, J., "Large-Scale Multidisciplinary Design Optimization of an eVTOL Aircraft using Comprehensive Analysis," Proceedings of the AIAA SciTech Forum, National Harbor, MD, January 23-27 2023.

2. Ruh, M., Fletcher, A., Sarojini, D., Sperry, M., Yan, J., Scotzniovsky, L., van Schie, S., Warner, M., Orndorff, N., Xiang, R., Joshy, A., Zhao, H., Krokowski, J., Gill, H., Lee, S., Cheng, Z., Cao, Z., Mi, C., Silva, C., Wolfe, L., Chen, J., and Hwang, J., "Large-scale Multidisciplinary Design Optimization of a NASA Air Taxi Concept Using a Comprehensive Physics-based System Model," Proceedings of the AIAA SciTech Forum, Orlando, FL, January 8-12 2024.

3. Lee, S., Ayton, L., Bertagnolio, F., Moreau, S., Chong, T. P., and Joseph, P., "Turbulent Boundary Layer Trailing-Edge Noise: Theory, Computation, Experiment, and Application," *Progress in Aerospace Sciences*, Vol. 126, 2021, pp. 100737. DOI: 10.1016/j.paerosci.2021.100737

4. Amiet, R., "Noise due to turbulent flow past a trailing edge," *Journal of Sound and Vibration*, Vol. 47, (3), 1976, pp. 387–393. DOI: 10.1016/0022-460X(76)90948-2

5. Li, S., and Lee, S., "Prediction of Urban Air Mobility Multirotor VTOL Broadband Noise Using UCD-QuietFly," *Journal of the American Helicopter Society*, Vol. 66, (3), 2021, pp. 1–13. DOI: 10.4050/jahs.66.032004

6. Li, S., and Lee, S., "Acoustic Analysis and Sound Quality Assessment of a Quiet Helicopter for Air Taxi Operations," *Journal of the American Helicopter Society*, Vol. 67, (3), 2022, pp. 1–15. DOI: 10.4050/jahs.67.032001

7. Lee, S., "Empirical Wall-Pressure Spectral Modeling for Zero and Adverse Pressure Gradient Flows," *AIAA Journal*, Vol. 56, (5), 2018, pp. 1818–1829. DOI: 10.2514/1.j056528

8. Lim, J., "Application of Parametric Airfoil Design for Rotor Performance Improvement," Proceedings of the 44th European Rotorcraft Forum, Delft, Netherlands, September 18–21, 2018.

9. Lim, J., Luke, A., Haehnel, R., and Dettwiller, I., "An Examination of Aerodynamic and Structural Loads for a Rotor Blade Optimized with Multi-Objective Genetic Algorithm," Proceedings of the 77th Annual Vertical Flight Society Annual Forum and Technology Display, Virtual, May 10–14, 2021.

10. Liu, C., and Lee, S., "Parametric Airfoil Design and Sensitivity Analysis for Turbulent Boundary-Layer Trailing-Edge Noise Reduction," *AIAA*, Vol. 60, (4), 2022, pp. 2324–2341. DOI: 10.2514/1.j060096

11. Lee, S., “The Effect of Airfoil Shape on Trailing Edge Noise,” *Journal of Theoretical and Computational Acoustics*, Vol. 27, (2), 2019, pp. 1850020. DOI: 10.1142/S2591728518500202

12. Liu, C., and Lee, S., “Surrogate-Based Optimization for Airfoil Trailing-Edge Noise Reduction Using Morphed Trailing-Edge Shapes,” Proceedings of Inter-noise 2020, Seoul, Korea, August 23-26, 2020.

13. Howe, M., *Acoustics of Fluid-Structure Interactions*, Cambridge University Press, Cambridge, England, UK, 1998.

14. Karimian, A., Paruchuri, C., and Joseph, P., “Optimised Propeller Geometries for Low Broadband Noise,” Proceedings of AIAA Aviation Forum, San Diego, CA, June 10–14, 2023.

15. Sobieczky, H., “Parametric Airfoils and Wings,” *Recent Development of Aerodynamic Design Methodologies*, Springer, 1999, pp. 71–87.

16. Kulfan, B. M., “Universal Parametric Geometry Representation Method,” *Journal of Aircraft*, Vol. 45, (1), January-February 2008, pp. 142–158. DOI: 10.2514/1.29958

17. Kou, J., Botero-Bolívar, L., Ballano, R., Marino, O., de Santana, L., Valero, E., and Ferrer, E., “Aeroacoustic airfoil shape optimization enhanced by autoencoders,” *Expert Systems with Applications*, Vol. 217, 2023, pp. 119513. DOI: https://doi.org/10.1016/j.eswa.2023.119513

18. Thurman, C., Boyd, D., and Simmons, B., “Comparison of Prediction Modeling Methodologies for Aeroacoustic Characterization of Hovering sUAS Rotors,” Proceedings of the AIAA Scitech Forum, National Harbor, MD Online, January 23-27 2023.

19. Brooks, T., Pope, D., and Marcolini, M., “Aifoil Self-Noise and Prediction,” Technical Report NASA Reference Publication 1218, National Aeronautics and Space Administration, 1989.

20. Ingraham, D., Gray, J. S., and Lopes, L. V., “Gradient-Based Propeller Optimization with Acoustic Constraints,” Proceedings of the AIAA Scitech Forum, San Diego, CA, January 7-11 2019.

21. Drela, M., “XFOIL: An Analysis and Design System for Low Reynolds Number Airfoils,” *Low Reynolds Number Aerodynamics*, edited by T. J. Mueller, Vol. 54, Springer, 1997.

22. Won, J., Trembois, N., and Lee, S., “Towards Accurate Broadband Noise Predictions Using CFD,” Proceedings of the 79th Annual Vertical Flight Society Forum and Technology Display, West Palm Beach, Florida, May 16–18, 2023.

23. Pettingill, N., Zawondny, N., Thurman, C., and Lopes, L., “Acoustic and Performance Characteristics of an Ideally Twisted Rotor in Hover,” Proceedings of AIAA Scitech Forum, Virtual, January 11–15 & 19–21, 2021.

24. Shum, J., and Lee, S., “Computational Study of Airfoil Design Parameters and Sensitivity Analysis for Dynamic Stall,” *AIAA Journal*, Vol. 62, (4), 2024, pp. 1611–1617. DOI: 10.2514/1.j063474

25. Della Vecchia, P., Daniele, E., and D’Amato, E., “An Airfoil Shape Optimization Technique Coupling PARSEC Parameterization and Evolutionary Algorithm,” *Aerospace Science and Technology*, Vol. 32, (1), 2014, pp. 103–110. DOI: 10.1016/j.ast.2013.11.006

26. Salunke, N., Ahamad, J., and Channiwala, S., “Airfoil Parameterization Techniques: A Review,” *American Journal of Mechanical Engineering*, Vol. 2, 2014, pp. 99–102. DOI: 10.12691/ajme-2-4-1

27. Lophaven, S. N., Nielsen, H. B., and Søndergaard, J., “DACE - A Matlab Kriging Toolbox, Version 2.0,” , 2002.

28. McKay, M. D., Beckman, R. J., and Conover, W. J., “A Comparison of Three Methods for Selecting Values of Input Variables in the Analysis of Output from a Computer Code,” *Technometrics*, Vol. 21, (2), 1979, pp. 239–245. DOI: 10.2307/1268522

29. Lee, H., Jo, Y., Lee, D.-J., and Choi, S., “Surrogate Model Based Design Optimization of Multiple Wing Sails Considering Flow Interaction Effect,” *Ocean Engineering*, Vol. 121, 2016, pp. 422–436. DOI: https://doi.org/10.1016/j.oceaneng.2016.05.051

30. Deb, K., *Multi-Objective Optimization using Evolutionary Algorithms*, John Wiley & Sons, Ltd, Chichester, England, 2001.

31. Chaderjian, N., “A Quantitative Approach for the Accurate CFD Simulation of Hover in Turbulent Flow,” *Journal of the American Helicopter Society*, Vol. 68, 10 2023. DOI: 10.4050/jahs.68.042009

32. Kang, D., and Lee, S., “Aeroacoustic Study of Morphed Trailing-Edge Airfoils Using Large-Eddy Simulations,” Proceedings of the 12th International Conference on Computational Fluid Dynamics, Kobe, Japan, July 14–19 2024.